

Quantum trajectory analysis of multimode subsystem-bath dynamics

Robert E. Wyatt and Kyungsun Na

Institute for Theoretical Chemistry, Department of Chemistry and Biochemistry, The University of Texas at Austin, Austin, Texas 78712

(Received 10 July 2001; published 18 December 2001)

The dynamics of a swarm of quantum trajectories is investigated for systems involving the interaction of an active mode (the subsystem) with an M -mode harmonic reservoir (the bath). Equations of motion for the position, velocity, and action function for elements of the probability fluid are integrated in the Lagrangian (moving with the fluid) picture of quantum hydrodynamics. These fluid elements are coupled through the Bohm quantum potential and as a result evolve as a correlated ensemble. Wave function synthesis along the trajectories permits an exact description of the quantum dynamics for the evolving probability fluid. The approach is fully quantum mechanical and does not involve classical or semiclassical approximations. Computational results are presented for three systems involving the interaction on an active mode with $M = 1, 10,$ and 15 bath modes. These results include configuration space trajectory evolution, flux analysis of the evolving ensemble, wave function synthesis along trajectories, and energy partitioning along specific trajectories. These results demonstrate the feasibility of using a small number of quantum trajectories to obtain accurate quantum results on some types of open quantum systems that are not amenable to standard quantum approaches involving basis set expansions or Eulerian space-fixed grids.

DOI: 10.1103/PhysRevE.65.016702

PACS number(s): 02.70.-c

I. INTRODUCTION

The analytical and computational analysis of a relatively small subsystem interacting with a multimode bath has an extensive history [1]. Because of computational limitations arising from the large number of degrees of freedom of the composite system, it has not been possible, except in special cases, to treat the full dynamical problem quantum mechanically. Traditional quantum mechanical approaches involving the use of square integrable basis sets or space-fixed grids quickly become intractable as the dimensionality of the system increases. Because of these restrictions, the analysis is frequently based upon a quantum subsystem interacting perturbatively or semiclassically with a classical harmonic bath. For example, semiclassical techniques have recently been applied to a double well potential and an anharmonic oscillator interacting with a bath of harmonic oscillators [2–6]. Frequently, the bath degrees of freedom are traced over and attention is focused upon the reduced density matrix for the subsystem. On the assumption that the coupling between the subsystem and the bath is bilinear in the subsystem and bath coordinates, the subsystem dynamics can be developed via the Feynman-Vernon influence functional [7–10] and by quantum master equations [11–16].

In this study, the subsystem-bath dynamics will be approached in a different way, from the viewpoint of the hydrodynamic formulation of quantum mechanics [17–22]. In this approach, trajectories (streamlines) for a number of elements of the probability fluid *for the entire system* will be developed. Elements of this quantum fluid are correlated through the nonlocal Bohm quantum potential, which is computed on the fly as the equations of motion are integrated to find the quantum trajectories. In addition, along these trajectories the subsystem-bath wave function may be computed. A unique feature of the hydrodynamic approach reported here is that the composite system (subsystem and bath) is treated quantum mechanically without the need for

imposing dynamical approximations. In addition, the computational effort is concentrated upon a relatively small number of fluid elements (quasiparticles) that form a moving nonuniform grid.

The type of subsystem-bath model that we will consider with the quantum trajectory method (QTM) [23–32] is exemplified by the potential energy surface displayed in Fig. 1.

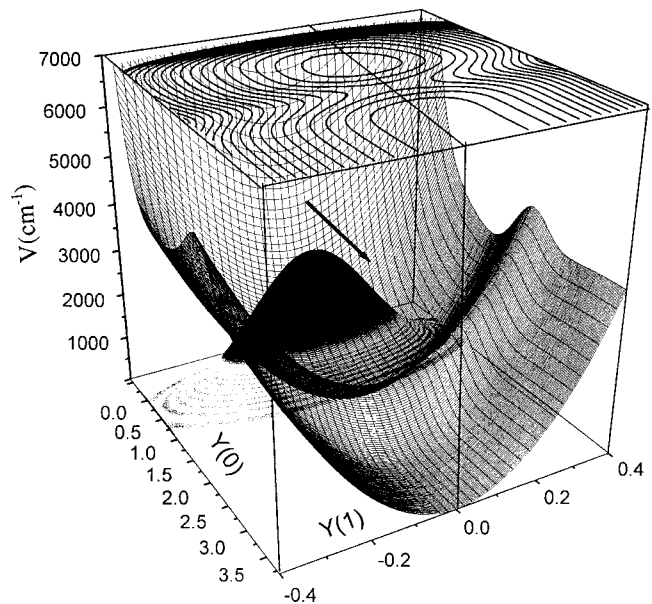


FIG. 1. A section through the potential energy surface for the $M = 10$ bath mode model. The wire mesh shows the potential energy in the y_0 (subsystem coordinate)- y_1 (bath mode number 1) subspace. The minimum barrier is 990 cm^{-1} and this occurs along the $y_0 = 2.0 \text{ a.u.}$ cut. The potential minimum in the interior valley (66 cm^{-1}) occurs at $y_0 = 1.16 \text{ a.u.}, y_1 = 0.04$. A contour map of the potential is shown in the top plane. The initial probability density for the Gaussian wave packet ($\times 800$) is shown centered at $y_0 = 2.0 \text{ a.u.}, y_1 = 0$.

Shown here is a slice through the potential surface for a ten bath mode system (this model is considered in more detail in Sec. IV B). The wire mesh potential surface is plotted above the coordinate plane spanned by y_0 (the subsystem coordinate) and y_1 (the first bath mode coordinate). A contour map of this potential is shown above the wire mesh in the upper horizontal plane. This potential is the sum of an exponential repulsive term and a repulsive Gaussian barrier along the subsystem coordinate and harmonic potentials for the ten bath modes, along with bilinear coupling terms (terms of the form $y_0 y_k$) that provide linkage between the subsystem and bath modes. In addition, this figure also shows the probability density for an initial Gaussian wave packet that is launched from the inner repulsive wall of the potential surface. The goal is to study the time evolution of elements of the probability fluid as they flow over the barrier region near $y_0=2$ a.u. out toward the asymptotic valley region ($y_0 \rightarrow \infty$).

The hydrodynamic formulation of quantum mechanics has its origins in the work of Madelung [17], de Broglie [18], Bohm and co-workers [19–21]. Studies in this area fall into two domains having different goals and methodologies. In the older of these approaches, the *analytical approach*, the equations of quantum hydrodynamics are used to *analyze the dynamics* of elements of the probability fluid *after* first solving the time-dependent Schrödinger equation to obtain the wave function. Examples of this approach include analyses of possible quantum chaos in stadium billiard problems [33–36], wave packet resonant scattering for the double barrier potential [30], vibrationally enhanced molecular breakup at a metal surface [37], the $E \otimes e$ Jahn-Teller problem [38], and wave packet dynamics for circular Rydberg states [39]. The second approach to quantum hydrodynamics is quite different; in the *synthetic approach*, the quantum hydrodynamic equations are solved *directly* to *predict* the space-time dynamics of elements of the probability fluid. The wave function is not precomputed as in the analytical approach; rather, it is developed on the fly during integration of the hydrodynamic equations.

The quantum trajectory method [23–29,31,32], QTM, is an example of the synthetic approach in which equations of motion for discretized fluid elements are formulated and solved in the Lagrangian, moving with the fluid, picture. The only approximation made in solving the hydrodynamic equations involves the use of a relatively small number of fluid elements. The QTM has been applied to barrier transmission [23,26], a collinear model chemical reaction [25], nonclassical reflection from a downhill ramp potential [27], and electronic nonadiabaticity in a two electronic state scattering problem [31,32]. As time goes on, the fluid elements generally form an unstructured grid and this presents computational difficulties in evaluating first and second derivatives of functions known only at the grid points. The moving weighted least squares algorithm [40–43] is one approach that has been utilized for derivative evaluation. In another approach, derivative evaluation has been performed using distributed approximating functionals [26] that have been extensively developed by Hoffman *et al.* [44].

In addition, Bittner and Wyatt [28,29] have presented sev-

eral enhancements to the hydrodynamic methodology, including techniques to deal with the node problem [29]. Near local regions where the quantum amplitude becomes very small, $R \rightarrow 0$, the quantum potential may become singular and as this occurs, another effect, referred to as inflation [45], sets in. Inflation is the tendency for fluid elements to move away from developing singularities, the nodes, with the result that “holes” develop in the density. From a computational viewpoint, this presents problems because of the low information density near the node and because of the highly unstructured mesh formed by the fluid elements. Adaptive regridding and change of representation from the hydrodynamic form of the wave function (involving R and S ; see Sec. III) to the real and imaginary form (involving A and B , where $A + iB = R e^{iS/\hbar}$) are techniques that may be used to deal with the node problem. So far, these techniques for handling the node problem have been tested and implemented only for one-dimensional barrier transmission problems.

In parallel with our development of the quantum trajectory method, Rabitz and co-workers [46–50] have also developed computational methods to integrate the quantum hydrodynamic equations in both the Eulerian and Lagrangian pictures. This quantum fluid dynamic (QFD) methodology has been applied to two-dimensional models of the photodissociation of NOCl and NO₂ [46,48] and to the optimal control of HCl in an external electric field [49]. In addition, radial basis functions were investigated for fitting of functions and evaluation of their derivatives in the Lagrangian picture [50]. Also, the Eulerian version of QFD was used to study the dynamics of Gaussian wave packets on four-dimensional quadratic potential surfaces [47].

Approximately 30 years before the QTM and the QFD were developed, Weiner and co-workers [51–55] introduced the first particle method for solving the quantum hydrodynamic equations. Applications made at that time were limited to Gaussian wave packets evolving on quadratic potential surfaces. It is important to recall that under these conditions, *the initial wave packet always remains Gaussian*, although spreading may occur at different rates along the different principal axes. The QTM and the QFD have the enormous advantage of permitting calculations beyond the paradigm “Gaussian packets/quadratic potentials.”

Other recent studies based upon the hydrodynamic formulation include the following: development of a quantum trajectory approach to the density matrix for dissipative systems [56], trajectory dynamics in the double well potential and in magnetic fields [57], the use of Delaunay tessellation for evaluation of the quantum potential [58], two approaches to mixed quantum-classical dynamics [59,60], and a classical limit of the Eulerian equations of motion for electronic nonadiabatic processes [61].

A different trajectory approach to quantum dynamics, termed “quantum dressed classical mechanics,” has been recently developed by Billing [62]. The center of a variable width Gaussian wave packet follows a classical trajectory. A time-dependent preexponential factor expressed in the discrete variable representation (DVR) brings in a set of grid points centered about the classical trajectory. These grid points explore a patch of space around the classical trajectory

and incorporate quantum corrections, including barrier tunneling. The trajectories followed by these DVR grid points are not Bohm trajectories, but there may be some correspondences between the two methods.

As we mentioned at the start of this section, the focus of this study concerns application of the quantum trajectory method to systems consisting of a subsystem interacting with a multimode harmonic bath. The subsystem itself may in general be multimode, but in this study the subsystem is described by a single mode for which the potential is an anharmonic function of position. The total number of modes considered in these models is far larger than have been considered in any previous fully quantum mechanical studies. The emphasis here is upon the trajectory dynamics; except for the first model in Sec. IV, averages over many trajectories are not performed. Computing averaged ‘‘observables’’ using the hydrodynamic methodology in systems of high dimensionality is certainly of interest. This important topic, along with analyses of dissipation and energy transfer, will be deferred to another part of this series.

In Sec. II of this study, the Hamiltonian for subsystem-bath models will be described, and anharmonic potentials will be defined for the three subsystems that are analyzed later in this study. In Sec. III, the hydrodynamic formulation of quantum mechanics will be reviewed, with emphasis upon the computation of trajectories followed by the fluid elements. In order to integrate the equations of motion, it is necessary to evaluate derivatives of functions whose values are known only on the unstructured mesh defined by the fluid elements. As in our earlier studies, the moving weighted least squares (MWLS) algorithm will be used for this purpose [40–43]. Some computational considerations connected with use of the MWLS will also be mentioned in Sec. III. Computational results on systems with 1, 10, and 15 bath modes will be presented in conjunction with the series of figures that are described in Sec. IV. The emphasis here will be upon the properties of a subset of trajectories that form part of the evolving quantum fluid. Finally, concluding remarks will be presented in Sec. V.

II. HAMILTONIAN FOR SUBSYSTEM-BATH MODELS

In this study, the one-dimensional subsystem, the active mode, is described by the coordinate y_0 and the M bath modes are described by the displacement coordinates $\{y_1, \dots, y_M\}$. The total system Hamiltonian is partitioned into subsystem, (harmonic) bath, and coupling contributions, $H = H_s + H_b + H_c$, where

$$H_s = \frac{1}{2m_0} p_0^2 + V(y_0), \quad (1)$$

$$H_b = \frac{1}{2} \sum_{i=1}^M \left\{ \frac{p_i^2}{m_i} + f_i y_i^2 \right\}, \quad (2)$$

$$H_c = \sum_{i=1}^M c_i(y_0) f_i y_0 y_i. \quad (3)$$

In the bath Hamiltonian, the force constants are related to the mode frequencies by $f_i = m_i \omega_i^2$. In the subsystem Hamil-

TABLE I. Parameters for the 2-mode model.

Mass for each mode (a.u.) m_i	2000, 2200
Center for each 1D wave packet (a.u.) y_i^0	0.4, 0.002
Harmonic bath frequencies (cm^{-1}) ω_i	1000, 2100
Width parameters for 1D Gaussian wave packets (a.u.) β_i	$\beta_0 = 4.556$, $\beta_1 = 10.525$
Subsystem-bath coupling constant (a.u.) c_i	0.0 (Fig. 2) -0.10 (Fig. 3) -0.17 and 0.00 (Fig. 4)
Falloff parameter for coupling constant $\gamma = 0.8$ a.u.	
Cutoff distance for coupling constant $\gamma_0^c = 1.0$ a.u.	
Initial subsystem kinetic energy $E_{\text{tr}}^0 = 10\,754$ cm^{-1}	
Cubic anharmonicity in subsystem potential $\alpha = -0.006\,92$	
Initial grid spacing along y_0 $\Delta y_0 = 0.015$ a.u.	
Time step for integration $\Delta t = 1$ a.u.	

tonian, three different anharmonic potentials were used, including a harmonic potential with cubic anharmonicity, an exponential repulsive potential, and a short-range exponential repulsive potential augmented with a Gaussian barrier

$$V_1(y_0) = \frac{1}{2} f_0 y_0^2 - \alpha y_0^3, \quad (4)$$

$$V_2(y_0) = A(e^{-\beta y_0} - 1), \quad (5)$$

$$V_3(y_0) = C e^{-\delta y_0} + D \exp[-\eta(y_0 - y_b)^2]. \quad (6)$$

For the potential V_2 , $V_2(y_0 \rightarrow \infty) \rightarrow -A$, and β is chosen so that the potential at $y_0 = -1$ has the input value V_0 . In Eq. (6), the barrier maximum for V_3 occurs when $y_0 = y_b$. Potentials V_1 , V_2 , and V_3 were used in the $M = 1, 15$, and 10 mode models, respectively.

Note that the M bath oscillators are not coupled among themselves. Quadratic coupling terms $y_i y_j$ could be included in future investigations. The coupling potential in Eq. (3) is bilinear in the subsystem-bath displacements $y_0 y_i$. In Sec. IV, mention will be made of calculations that include higher-order subsystem-bath coupling terms (of the form $y_0 y_i^2$). In order to prevent these coupling terms from becoming arbitrarily large as y_0 increases, the coupling coefficients c_i were damped when y_0 exceeds a cutoff value. For the $M = 1$ and 10 models, $c_i = c_i^0$ when $y_0 < y_0^c$ and $c_i = c_i^0 \exp[-\gamma(y_0 - y_0^c)^2]$ otherwise. For the $M = 15$ model, a sharp cutoff function was used, $c_i = c_i^0$ when $y_0 < y_0^c$ and $c_i = 0$ otherwise. The parameters used in the Hamiltonians for these models are listed in Tables I–III; further details are provided later in Sec. IV when the computational results are described.

TABLE II. Parameters for the 11-mode model.

Mass for each mode (a.u.) m_i	2000, 2200, 2400, 2600, 3000, 3200, 3400, 3600, 3700, 3800
Center for each 1D wave packet (a.u.) y_i^0	0.4, 0.006, 0.0, 0.001, 0.002, -0.002, 0.005, -0.005, 0.0, 0.0, 0.005
Harmonic bath frequencies (cm^{-1}) ω_i	2100, 1700, 1800, 1900, 2100, 2200, 2300, 2100, 2300, 2400
Width parameters for 1D Gaussian wave packets (a.u.) β_i	$\beta_0=3.0$, $\beta_i=(1/2)m_i\omega_i$ $i=1,2,\dots,10$
Subsystem-bath coupling constants (a.u.) c_i	-0.03, -0.02, 0.03, -0.02, 0.03, -0.02, -0.03, -0.02, -0.02, 0.03
Falloff parameter for coupling constants $\gamma=0.8$ a.u.	
Cutoff distance for coupling constants $y_o^c=1.0$ a.u.	
Initial subsystem kinetic energy $E_{\text{tr}}^0=1500$ cm^{-1}	
Parameters for subsystem potential	$C=100$ cm^{-1} , $D=1000$ cm^{-1} , $\delta=0.3$ a.u., $\eta=5.0$ a.u.
Initial grid spacing along y_0	$\Delta y_0=0.015$ a.u.
Time step for integration	$\Delta t=1$ a.u.

III. QUANTUM TRAJECTORY METHOD

A. Quantum hydrodynamic equations

In this section, a brief review will be presented of the equations needed to implement the quantum trajectory method [23–32]. The hydrodynamic formulation is initiated by substituting the polar form of the time-dependent wave function (this is the Madelung transform [17]), $\Psi(y,t) = R(y,t)\exp[iS(y,t)/\hbar]$, into the Schrodinger time-dependent wave equation. In this amplitude-phase decomposition, the real-valued amplitude and action functions are denoted R and S . An advantage of this representation is that R and S are frequently slowly varying functions of position. In terms of R and S , the probability density and the local flow velocity are given by $\rho=R^2$ and $v=(\nabla S)/m$. After separating into real and imaginary parts, and then introducing the Lagrangian time derivative, $df/dt = \partial f/\partial t + v \cdot \nabla f$, we obtain the equations of motion

$$\frac{d\rho}{dt} = -\rho \nabla \cdot v, \quad (7)$$

$$\frac{dv}{dt} = -\frac{1}{m} \nabla(V+Q). \quad (8)$$

Equation (7) is recognized at the Lagrangian version of the continuity equation, in which the rate of change in the density along a streamline is related to the divergence of the velocity field. Equation (8) is a Newtonian-type equation in which the flow acceleration is produced by two force terms on the right side. The classical force acting on the fluid element is $f_c = -\nabla V$, and the quantum force is given by $f_q = -\nabla Q$. In these equations, V is the potential energy func-

TABLE III. Parameters for the 16-mode model.

Mass for each mode (a.u.) m_i	1000, 1250, 1628, 1253, 1708, 1711, 1529, 1425, 1573, 1602, 1342, 1636, 1310, 1340, 1583, 1358
Center for each 1D wave packet (a.u.) y_i^0	0.08, 0.002, -0.005, 0.003, 0.0, -0.005, 0.002, 0.007, 0.008, -0.001, 0.003, 0.002, -0.006, 0.003, 0.001, 0.009
Harmonic bath frequencies (cm^{-1}) ω_i	6000, 3250, 1083, 1742, 3263, 3662, 1907, 1975, 398, 449, 2003, 1914, 2917, 734, 2972
Width parameters for 1D Gaussian wave packets (a.u.) β_i	8.9, 18.8, 13.3, 3.4, 7.5, 14.0, 14.0, 6.8, 7.8, 1.6, 1.5, 8.2, 6.3, 9.1, 2.9, 10.1
Subsystem-bath coupling constants (a.u.) c_i	0.037, -0.02, 0.03, 0.043, -0.045, 0.01, -0.009, -0.002, -0.047, 0.03, 0.026, -0.036, -0.029, -0.011, 0.043
Cutoff distance for coupling constants $y_o^c=2.0$ a.u.	
Initial subsystem kinetic energy $E_{\text{tr}}^0=0$	
Parameters for subsystem potential	$A=1000$ cm^{-1} , $V_0=5000$ cm^{-1} , $\beta=\ln(1+V_0/A)$
Initial grid spacing along y_0	$\Delta y_0=0.06$ a.u.
Time step for integration	$\Delta t=1$ a.u.

tion and Q is the time-dependent Bohm quantum potential [19–21]. If Q is neglected in Eq. (8), the classical dynamics of an ensemble is recovered.

The Bohm potential depends upon the Laplacian of the amplitude and is given by

$$Q(y,t) = -\frac{\hbar^2}{2m} \frac{1}{R(y,t)} \nabla^2 R(y,t) = -\frac{\hbar^2}{2m} \rho^{-1/2} \nabla^2 \rho^{1/2}. \quad (9)$$

It is worth noting that the quantum potential is identical to the local shape (as opposed to flow) kinetic energy associated with the wave packet. The local kinetic energy is defined by [22]

$$T_{\text{local}} = -\frac{\hbar^2}{2m} \text{Re} \left\{ \frac{\Psi^* \nabla^2 \Psi}{\Psi^* \Psi} \right\}. \quad (10)$$

The kinetic energy defined in this way may be partitioned [24] $T_{\text{shape}} + T_{\text{flow}}$, where the flow kinetic energy arises from the gradient of the action function and is given by $T_{\text{flow}} = (\nabla S)^2/(2m)$. The shape kinetic energy is then given by the difference $T_{\text{shape}} = T_{\text{local}} - T_{\text{flow}}$ and this quantity is identical to the quantum potential, Q , in Eq. (9). Computation of the quantum potential in Eq. (9) is rendered more accurate if derivatives are evaluated for the exponentiated amplitude [23,46], $R = \exp(C)$, where C is referred to as the C amplitude. In terms of derivatives of the C amplitude, the quantum potential is

$$Q = -\frac{\hbar^2}{2m}[\nabla^2 C + (\nabla C)^2]. \quad (11)$$

The advantage of working with C amplitude is that this quantity may frequently be fit with high accuracy by a low degree polynomial; this is not generally true for R itself.

Closure of the set of dynamical equations is obtained by introducing the Lagrangian equation of motion for the action function [24],

$$\frac{dS}{dt} = \frac{1}{2m}(\nabla S)^2 - (V + Q) = L_{\text{quantum}}. \quad (12)$$

The right side defines the quantum Lagrangian. It measures the excess of the kinetic energy flow over the total potential energy, which in turn is the sum of the potential V and the quantum potential.

Equations (7), (8), and (12) along with the definition of Q in Eq. (11) constitute the defining equations for the quantum trajectory method. No approximations were made in deriving these equations from the time-dependent Schrödinger equation. However, in order to implement these equations, an approximation will be made. The initial wave packet will be subdivided into N fluid elements and the equations of motion will be used to find the position, flow velocity, probability density, and action function along the trajectories followed by these elements. The flow of these fluid elements through phase space is that of a compressible fluid (generally, $\nabla \cdot v \neq 0$).

From the density and action functions computed along each trajectory, the wave function may be synthesized [24]. Given the wave function $\Psi(y_0, t_0)$ at position y_0 at time t_0 , the wave function along the trajectory $y(t)$ developed by this fluid element is

$$\begin{aligned} \Psi(y, t) = & \exp\left(-\frac{1}{2} \int_{t_0}^t \nabla \cdot v dt\right) \\ & \times \exp\left[-\int_{t_0}^t L_{\text{quantum}}(t) dt\right] \Psi(y_0, t_0). \end{aligned} \quad (13)$$

In this equation, the first exponential updates the R amplitude along the trajectory. This term is obtained by analytic integration of Eq. (7) for the density followed by taking the square root to obtain $R(y, t)$. The second exponential in Eq. (13) updates the action function along the trajectory. This term is obtained by integrating Eq. (12) for dS/dt along the trajectory. An important feature of Eq. (13) is that a *single trajectory* makes the trip from (y_0, t_0) to (y, t) . A complicated summation over contributions from trajectories arriving along different space-time paths is not required.

The self-consistency of the hydrodynamic equations embodies de Broglie's pilot wave concept [18]. The wave function determines the motion of the fluid elements through the quantum force, which in turn is a function of the density, Eqs. (7) and (8), and this evolving ensemble of fluid elements in turn determines the new value for the wave function at the position of each fluid element, Eq. (13).

One final feature to mention concerns the two noncrossing rules [22]: (1) quantum trajectories cannot pass through the same space-time point; (2) quantum trajectories cannot puncture through nodal surfaces.

B. Trajectories for fluid elements

The Lagrangian equations of motion are used to update the *descriptor* for each of the N fluid elements. At each time step, the descriptor for each fluid element stores the position, velocity, C amplitude, and action function, $\Delta_i(t) = \{y_i, v_i, C_i, S_i\}$. Each fluid element follows a trajectory that may be viewed in both configuration and phase space. In addition, the wave function along each trajectory may be found from the known values of C and S ; for example, for the i th fluid element, $\ln \Psi_i = C_i + iS_i/\hbar$.

If the number of bath modes is small, say $M \leq 3$, then at $t=0$ it is convenient to start out the coordinates for each fluid element on a Cartesian grid. However, for a larger number of bath modes, it is neither necessary nor useful to do this. In the studies reported here, we first set up an N point uniform grid along the y_0 axis. For each of these points, a random value is then selected for each of the M bath coordinates. Each coordinate is restricted to the region $|y_i| \leq y_i^{\text{max}}$, where the maximum value is chosen so that the wave function for this mode is greater than about 0.01. In this way, each fluid element is assigned $M+1$ initial coordinates and when viewed in the $M+1$ dimensional coordinate space, the ensemble of N fluid elements forms an irregular mesh.

For the system-bath problems studied here, it is not necessary to cover each coordinate direction with a large number of points, thus forming (at $t=0$) a rectangular lattice in the $(M+1)$ -dimensional space. In this unfavorable case, the total number of points would scale roughly as $\langle N \rangle^{(M+1)}$, where $\langle N \rangle$ is the average number of points along each axis. It would be reasonable to expect that $\langle N \rangle > 10$. If this were the case, the $M=10$ and 15 mode systems used in this study would be beyond current computational capabilities. For the computations reported later, the values of $\langle N \rangle$ are 1.4 and 1.6 for the $M=15$ and 10 bath mode systems, respectively. From the viewpoint of traditional space-fixed grid calculations, these values are startlingly low.

At $t=0$, the initial wave function is assumed to be factorizable into the product of $M+1$ normalized Gaussian (one-dimensional) wave functions times a translational function (a plane wave) that specifies the initial action function

$$\begin{aligned} \Psi(y, t=0) = & \prod_{i=0}^M (\beta_i/\pi)^{1/4} \exp[-\beta_i(y_i - y_i^0)^2] \\ & \times \exp[iS(y_0, t=0)/\hbar]. \end{aligned} \quad (14)$$

The width parameters β_i and the centers y_i^0 will be specified later when the computational results are presented. For the $M=15$ model, the initial wave packet is chosen to be stationary, $S(y, t=0)=0$. For the $M=1$ and 10 models, the wave packet is launched with an initial momentum in the $+y_0$ direction, $S(y_0, t=0) = (2m_0 E_{\text{tr}}^0)^{1/2} (y_0 - y_0^0)$, where E_{tr}^0 is the initial translational energy. Although the wave function in Eq. (14) is a multidimensional Gaussian, there is no re-

quirement in the subsequent dynamics that the total wave function be either factorizable or Gaussian in any degree of freedom.

C. Least squares fitting and computation of derivatives

Given a function $f(y)$ specified only at N points in the $(M+1)$ -dimensional space $\mathbb{R}^{(M+1)}$, it is necessary to evaluate first and second derivatives at these points in order to integrate the equations of motion. The quantities that need to be evaluated at the positions of the fluid elements are ∇C , $\nabla^2 C$, ∇Q , and $\nabla \cdot v$. In order to evaluate these derivatives, we will use the same algorithm that has been used in earlier applications of the QTM, namely, the MWLS algorithm. In order to perform the fit around point (fluid element) j , we first select a set of n_p nearest neighbor points (including the ‘‘central’’ point j), these points define the stencil. Within this stencil, the function is expanded in a set of n_b local basis functions $\{p_k(y-y_j)\}$,

$$f(y) = \sum_{k=1}^{n_b} a_k(t) p_k(y-y_j), \quad (15)$$

where the expansion coefficients $\{a_k\}$ depend upon the time at which the fit is performed and they are found by solving a system of linear algebraic equations. The accuracy of the local fit is determined by the number and nature of the basis functions in addition to the number of points included in the stencil. In order to restrict the field of view, a Gaussian weight function centered at point j is used. Once the expansion coefficients have been determined, the partial derivatives of order n may be evaluated directly at the position of the central node

$$\frac{\partial^{(n)} f}{\partial y_1^{(n)}} = \sum_{k=1}^{n_b} a_k \left(\frac{\partial^{(n)} p_k}{\partial y_1^{(n)}} \right). \quad (16)$$

Because the basis functions are monomials, only a single term survives on the right side of this equation.

In this study, it will be assumed that the input function can be accurately fit around point y^0 by basis set \mathbf{B} consisting of monomials of degree less and equal to 2, including the constant term $\{1\}$, linear terms $\{z_0, z_1, \dots\}$, diagonal quadratic terms $\{z_0^2, z_1^2, \dots\}$, and off-diagonal quadratic terms $\{z_0 z_1, z_1 z_2, \dots\}$, where the z_i are local displacement coordinates, $z_i = y_i - y_i^0$, $i = 0, 1, \dots, M$. For the space $\mathbb{R}^{(M+1)}$, the dimension of \mathbf{B} is given by $n_b = 1 + 2(M+1) + M(M+1)/2$. For example, for the $M = 10$ model considered later, $n_b = 78$, and for the $M = 15$ model, $n_b = 153$. Since the number of basis functions increases as M^2 , it is not efficient to use this type of polynomial basis for $M > 15$ (although we have done some computations with $M = 20$).

In practice, both the C amplitude and the action function are fit to the previously mentioned basis set expressed in displacement coordinates. As a result, the *local fit to the wave function* near point y^0 is given by the complex Gaussian function

$$\Psi(y; y^0) = \exp[c_0 + c_1(y - y^0) + (y - y^0)^t c_2 (y - y^0)],$$

in which $(y - y^0)$ is the $(M+1)$ -dimensional displacement vector, c_0 and c_1 are complex-valued coefficient vectors, and

c_2 is an $(M+1)$ -dimensional (complex-valued) square matrix. This local Gaussian fit does not constrain the overall (global) wave function to being Gaussian in shape.

D. Computational considerations

Approximately 90% of the computational effort involved in advancing one time step is spent in the least squares fitting procedure. In order to improve the efficiency of this procedure, two techniques were employed to reduce the number of arithmetic operations. First, in order to find the $(n_p - 1)$ ancillary points surrounding the central point in the stencil, an index array is generated to sort the points by increasing distance from the central point. In order to reduce the number of operations, this index array is generated once every Δ_{sort} time steps rather than at the start of every time step. (In practice, $\Delta_{\text{sort}} = 20$ was used.) This increment must be decreased if and when the dynamics is complicated by fluid elements changing their relative positions.

The least squares procedure was accelerated by abandoning at each time step the direct solution (using Gaussian elimination, GE) of the algebraic equations for the expansion coefficients $\{a_k\}$ used in Eq. (15). In matrix notation, the equations for these coefficients have the form $[40] \mathbf{B}\mathbf{a} = \mathbf{c}$, where \mathbf{B} is an $n_b \times n_b$ square matrix, and \mathbf{a} and \mathbf{c} are $n_b \times 1$ column vectors. Matrices \mathbf{B} and \mathbf{c} are known in terms of the local basis functions and the input function values evaluated at all points of the stencil. Rather than directly solving these matrix equations at each time step, an iterative procedure was used. If we partition the square matrix into diagonal (\mathbf{D}), lower triangular (\mathbf{L}), and upper triangular submatrices (\mathbf{U}), the matrix equation may be rewritten $\mathbf{D}\mathbf{a} = \mathbf{c} - (\mathbf{L} + \mathbf{U})\mathbf{a} = \mathbf{c} - (\mathbf{B} - \mathbf{D})\mathbf{a}$. This suggests the following simple iterative scheme (Jacobi iteration) for the vector \mathbf{a} ,

$$\mathbf{a}^{k+1} = \mathbf{D}^{-1}[\mathbf{c} - (\mathbf{B} - \mathbf{D})\mathbf{a}^k], \quad (17)$$

where the first vector \mathbf{a}^1 must be specified to prime the iterative process. If the newly generated components of \mathbf{a}^{k+1} are used on the right side as soon as they are computed, this algorithm is referred to as Gauss-Seidel iteration (GSI). Altogether, k_{max} iteration steps are used, this number is found by monitoring the change in the iteration vector as k increases. This iteration procedure is implemented in the quantum trajectory program in the following way: (1) the direct algorithm based upon GE is used to generate the initial vector \mathbf{a}^1 ; (2) this vector is then used to iteratively generate the solution vectors for the following Δ_{GS} time steps. At this point, a fresh solution vector is generated using GE.

In test calculations for a model with $M = 4$ bath modes using $N = 101$ fluid elements, 21 quadratic basis functions in the local fit, 30 points in the stencil, and $k_{\text{max}} = 10$ Gauss-Seidel iterations, the speedup (in %) using Δ_{GS} iterations is defined as $S(\Delta_{\text{GS}}) = 100[T_{\text{direct}} - T_{\text{iterative}}(\Delta_{\text{GS}})]/T_{\text{direct}}$, where the numerator is the saving in CPU time and the denominator is the time for the noniterative (direct) calculation. As Δ_{GS} increases, the accuracy of the quantities stored in the descriptor gradually decreases. To counter this tendency, Δ_{GS} was kept relatively low, in the range 2–5. This led to savings in CPU time in the range 20–30%.

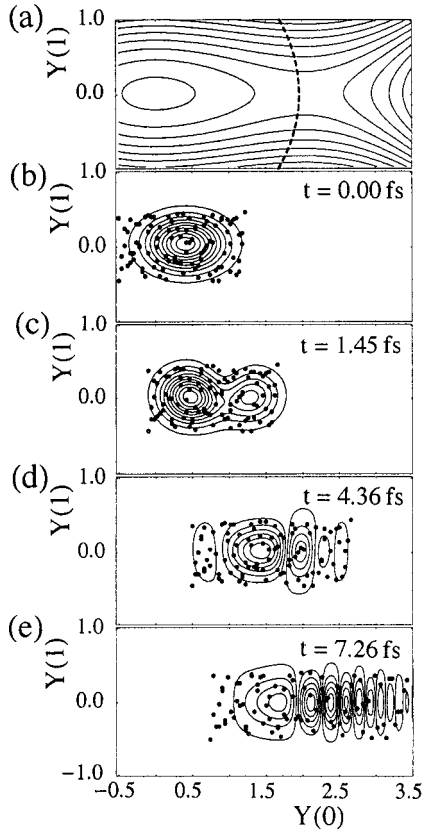


FIG. 2. (a) Contour map of the potential energy surface for the $M=1$ model. The subsystem-bath coupling coefficient has been set to zero. The circular dashed curve is the surface across which the flux is calculated. Parts (b)–(e) show the time development of the fluid elements (dots). In addition, contours of the real part of the wave function (interpolated from the values at the dots) are shown.

IV. COMPUTATIONAL RESULTS

A. The $M=1$ dissociative model: Wave function and flux analysis

Our first application involves an anharmonic oscillator interacting with a single bath mode. Parameters for the Hamiltonian used in this model are given in Table I and contour maps of the potential surfaces in the absence of subsystem-bath coupling ($c=0$) and with coupling ($c=-0.10$) are shown in Figs. 2(a) and 3(a), respectively. The subsystem potential $V_1(y_0)$ consists of a cubic anharmonic term added to a harmonic potential. The local minimum of the potential lies at $y_0=y_1=0$ and has the value zero. In Fig. 2(a), the saddle point occurs at $y_0=2.0$ a.u., $y_1=0$ and has the value 6077 cm^{-1} , while in Fig. 2(b), the saddle point occurs at $y_0=2.04$ a.u., $y_1=0.09$ a.u., and has the value 5906 cm^{-1} . Also shown in these figures is a dashed curve (a circle of radius $r=2$ a.u.) across which the flux will be calculated. Also note in Fig. 3(a) that the principal axis of the potential energy surface is tilted in the counterclockwise direction ($\theta=0.042$ rad) due to the coupling term in the potential.

In Figs. 2 and 3, the time dependence of the fluid elements (large dots) are shown along with contour maps displaying the real part of the wave function, $\text{Re}[\Psi(y_0, y_1)]$

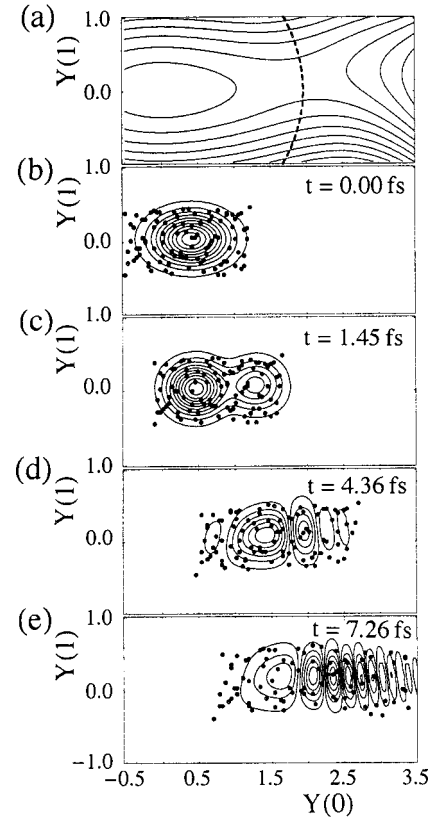


FIG. 3. (a) Contour map of the potential energy surface for the $M=1$ model. The subsystem and the bath are coupled ($c=-0.10$). The circular dashed curve is the surface across which the flux is calculated. Parts (b)–(e) show the time development of the fluid elements. In addition, contours of the real part of the wave function are shown.

$=R(y_0, y_1)\cos[S(y_0, y_1)/\hbar]$. Although this quantity oscillates along the y_0 coordinate, nodes do not develop in the density. These figures were generated from the descriptors carried by the nodes by the following procedure. Since the C amplitude ($R=e^C$) and the action (S) are known only at the positions of the fluid elements, it is necessary to interpolate (using MWLS) from this irregular grid onto a uniform mesh covering the display region before invoking the contour routine. An important feature of the Lagrangian formulation is apparent from these figures, smoothed quantities can be interpolated from information available at a relatively small number of points on the irregular mesh. When we go to systems with higher dimensionality, this advantage becomes even more significant.

From information carried in the descriptors for the fluid elements, average values of dynamical quantities may be calculated. For example, the following expression is used to calculate the time dependence of the rate of flow of probability across a boundary surface (Σ)

$$R(t) = \int_{\Sigma} j \cdot n dA, \quad (18)$$

where n is an outward directed unit normal vector, $j = \rho v$, and dA is an element of area. In addition, the time integral of the rate gives the decay probability from the initial localized state

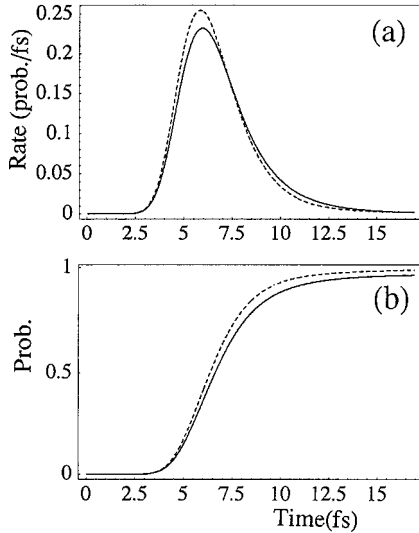


FIG. 4. (a) Rate of flow of probability across the boundary surface (dashed lines in Figs. 2 and 3) and (b) time integral of the rate, the decay probability. The continuous curve corresponds to the non-coupling case shown in Fig. 2 and the dashed curve was obtained using the coupling coefficient $c = -0.17$.

$$\text{Prob}(t) = \int_0^t R(\tau) d\tau. \quad (19)$$

In order to obtain a continuous flux (ρv) from the descriptors carried by the discrete fluid elements flowing across Σ , it is necessary to interpolate the density and velocity carried by the fluid elements onto the boundary surface. Using this technique, flow rates and decay probabilities were calculated and these are shown for in Fig. 4 for two cases, no subsystem-bath coupling (continuous curves) and for a system where coupling is included (dashed curves, for $c = -0.17$). [A different value for the coupling constant (c) was used in this figure compared to Fig. 3 in order to obtain larger differences in the flux and probability between the $c = 0$ and $c \neq 0$ cases.] By 12.5 fs, the flow rate has decreased to about 3% of the maximum value, and the decay probability has increased to about 0.93.

B. The $M=10$ barrier model

In Sec. I, reference was made to the potential energy surface and the initial wave packet for the $M=10$ system shown in Fig. 1. The parameters used in this potential along with other quantities needed to specify the model are listed in Table II. The bath mode frequencies ω_1 range from 1700 to 2400 cm^{-1} and the masses range from 2000 to 3800 a.u. For this model, the initial wave packet was discretized into $N=101$ fluid elements and the Lagrangian hydrodynamic equations were integrated for 1200 time steps ($\Delta t = 1 \text{ a.u.} = 0.024 \text{ fs}$). The initial wave packet was launched from the inner repulsive wall of the potential with a translational energy of 1500 cm^{-1} and with the initial momentum in the $+y_0$ direction. Each time step in the numerical integration of the equations of motion required about 7 sec of CPU time on one processor of the Cray SV1.

1. Density and velocity maps

Figure 5 shows velocity maps for the N particles in the (y_0, y_1) subspace at three times (a) $t=0$, (b) $t=9.5 \text{ fs}$, and (c) $t=14.25 \text{ fs}$. The size of the ball at the tail of each velocity vector is related nonlinearly to the density carried by that particle. [The radius of the ball is given by $r = A(\rho/\rho_{\max})^{(0.1)}$, where ρ_{\max} is the largest value of the density at this time step.] The velocity vectors shown here are projections of the $M+1$ component vectors into the (y_0, y_1) plane. In part (a), all vectors are of the same length and they are directed along the $+y_0$ axis, this is in accord with the initial condition. In part (b), 28 of the fluid elements have crossed the barrier at $y_0=2 \text{ a.u.}$ and they are starting to accelerate downhill into the asymptotic valley. The velocity vectors are shorter for the remaining fluid elements that are still decelerating on the uphill side of the barrier ($y_0 < 2 \text{ a.u.}$). In part (c), many of the fluid elements have picked up small velocity components along the y_1 direction, this represents energy transfer to the bath from the subsystem mode y_0 . Also, by this time step, 69 of the fluid elements have made it over the barrier.

2. Trajectory evolution

The configuration space-time evolution for five trajectories from this ensemble are plotted in Fig. 6. In this figure, the time dependence of the (y_0, y_1) coordinate pair is shown for trajectories 20, 40, 60, 80, and 100. In addition, the projection of trajectory 100 onto the three coordinate planes is also shown. Trajectories 20 and 100 are launched from near the back and front ends (larger value for y_0) of the swarm, respectively. It is evident that trajectories 20, 40, and 60 decelerate as they approach the barrier region (this occurs at about $t=15 \text{ fs}$) and that trajectories 80 and 100 accelerate quickly to larger values of y_0 after crossing the barrier.

3. Wave function synthesis along trajectories

We mentioned in Sec. III A that the wave function can be synthesized along each trajectory as it evolves through the $(M+1)$ -dimensional space. The three-dimensional plots displayed in Fig. 7 show the time dependence of the wave function for two trajectories selected from the ensemble. For each horizontal time slice, the radial distance from the vertical axis is $\rho^{1/2}$ and the twist of the parametrized function $\Psi(t)$ around this axis is generated by the phase $S(t)/h$. Figure 7(a) for trajectory 72 shows gradually increasing density as the trajectory moves toward the barrier maximum that is reached for times near the top of the figure. Figure 7(b) for trajectory 45 shows an increase of density near 15 fs, but the density starts to decrease as the trajectory begins accelerating on the downhill side of the barrier (near $t=20 \text{ fs}$).

4. Dynamical analysis

Further dynamical analysis for trajectory 72 is shown in the four parts of Fig. 8. Figure 8(a) displays the y_0 components of the forces acting on this fluid element. Reference to Eq. (8) shows that the acceleration of a fluid element is due to the “classical” force arising from the gradient of the po-

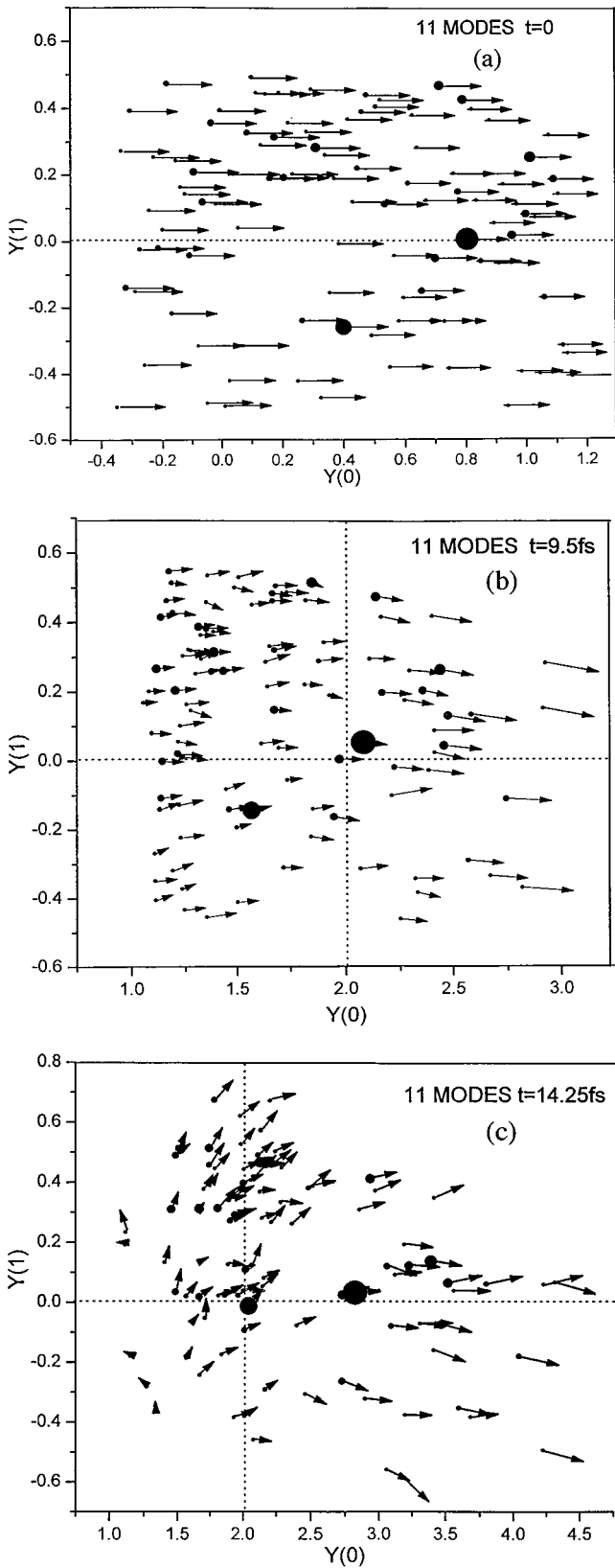


FIG. 5. Velocity maps projected into the (y_0, y_1) plane at three times: (a) $t=0$, (b) $t=9.5$ fs, and (c) $t=14$ fs. The radius of the ball at the tail of each vector is proportional to the density carried by this fluid element. The vertical dotted line shows the position of the barrier maximum.

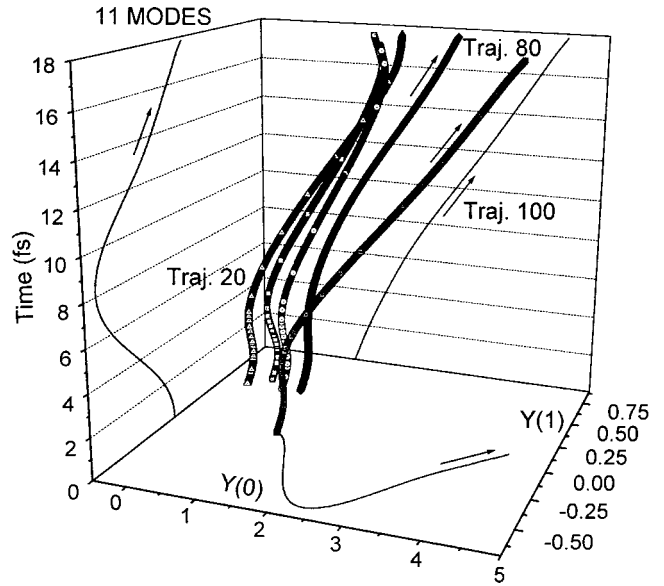


FIG. 6. Time dependence of trajectories 20, 40, 60, 80, and 100 in the (y_0, y_1) plane. The projections of trajectory 100 upon the three coordinate planes are also shown. Trajectory 100 is associated with a fluid element near the leading edge of the wave packet.

tential V acting in concert with the quantum force arising from the gradient of the quantum potential Q . The time dependence of both components of these forces are shown in Fig. 8(a). During some time intervals, the classical and quantum forces act together in the same direction, but at other times they work to oppose each other. The classical force is positive from $t=0$ until 4.5 fs and remains negative for the remaining times shown in this figure. The quantum force is positive until 2.1 fs, becomes negative until 8.3 fs, and then becomes positive again until 15.9 fs. What is, at first, surprising about the classical force is that this fluid element is moving downhill on the potential $V_2(y_0)$ until 3.2 fs and then uphill toward the barrier maximum that is reached at 11.6 fs. Thus for part of the time that the fluid element is moving uphill, between 3.2 and 4.5 fs, the classical force is negative, directed away from the barrier maximum. The origin of this odd feature is that the classical force is made up of two components, the “pure” mode-zero component [arising from the gradient of $V_2(y_0)$] and a contribution from the gradient of the coupling term. During some time intervals, these two contributions have opposite signs and partially cancel.

Continuing with the analysis for trajectory 72, Fig. 8(b) shows the time dependence of the potentials V and Q . Starting at $t=0$, V decreases for the first 6 fs, then gradually increases when the trajectory moves uphill toward the barrier maximum. At 11.6 fs, the barrier is crossed, but V (the total potential energy) does not decrease because a fraction of the potential energy is stored in the bath modes. Figure 8(c) shows the time dependence of the total potential energy, $V + Q$, and the kinetic energy, KB . The kinetic energy initially increases while $V + Q$ decreases. The kinetic energy then decreases for the first part of the uphill journey. The kinetic energy begins to increase before the barrier maximum when the bath modes acquire energy. Finally, Fig. 8(d) shows the

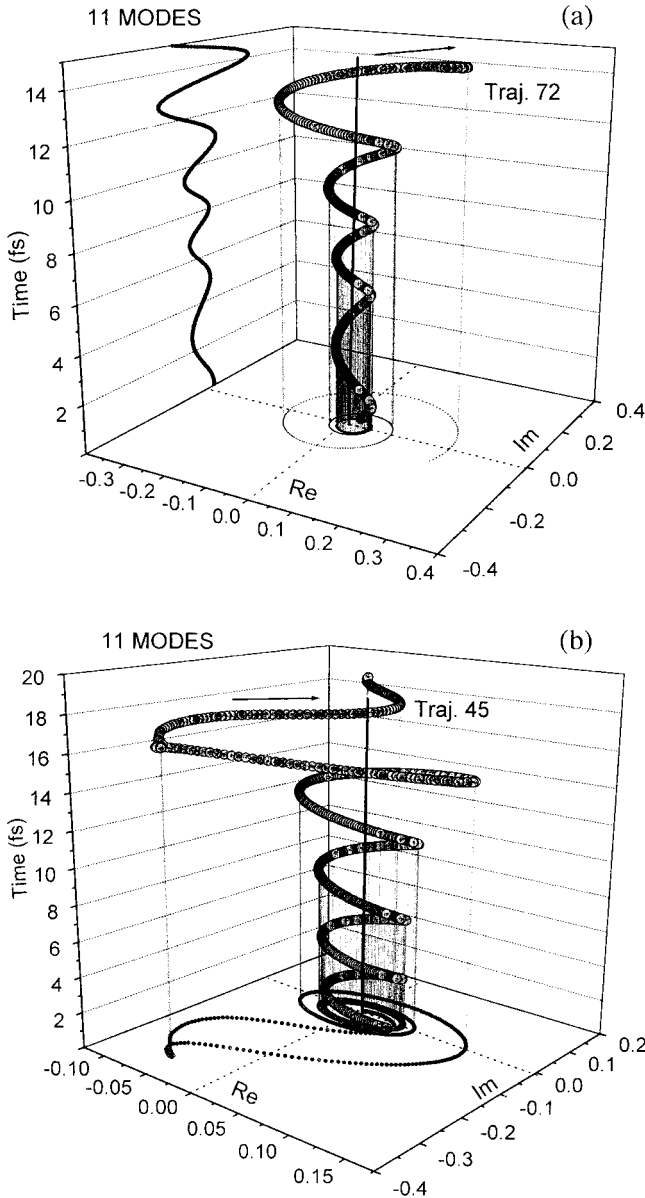


FIG. 7. Time dependence of the wave function for trajectories 72 [part (a)] and 45 [part (b)]. The real and imaginary parts of the wave function are plotted vs time. At each time, the radius of the cylinder is $\rho^{1/2}$ and the phase angle is S/\hbar .

action function and the quantum Lagrangian [see Eq. (12)]. The quantum Lagrangian is negative at all times because the kinetic energy remains lower than the total potential energy, as shown in Fig. 8(c). The action function starts out positive, but becomes increasingly negative as time increases because of the negative values for L_{quantum} .

5. Higher-order coupling

Most studies of subsystem-bath dynamics use the bilinear coupling potential in Eq. (3). In order to investigate the effect of higher-order coupling terms, a cubic coupling potential was added to the bilinear term. This coupling potential is given by

$$H_c^{\text{cubic}} = \sum_{i=1}^M d_i(y_0) f_i y_0 y_i^2, \quad (20)$$

Again, the coupling coefficients are damped at large values of y_0 using the same damping function as for the bilinear coupling term. In this study, the coefficients are given by $d_i = (-1)^j \zeta$ (where $\zeta = 0.1$ a.u.) and this is multiplied by the exponential damping function when y_0 exceeds a cutoff value. Similar to Fig. 6 for the bilinear coupling case, Fig. 9(a) shows the time dependence of the (y_0, y_1) coordinate pair for five trajectories, numbers 20, 40, 60, 80, and 100. Both the bilinear and the cubic coupling potentials were included in the dynamics. Over the 20 fs time scale shown in this figure, only trajectory 20 fails to make it over the barrier. After surmounting the barrier, the trajectories quickly accelerate toward the asymptotic valley.

6. Random coupling

In the previous calculations, once the sets of coupling coefficients $\{c_i\}$ and $\{d_i\}$ were specified at $t=0$, they remained constant throughout the time evolution of the trajectories. However, it is possible to impart a time dependence to these coefficients, to simulate a fluctuating linkage between the subsystem and the bath. In another set of calculations, every Δ_r time steps, the signs and magnitudes of the coefficients were varied randomly. In particular, the coefficients were chosen according to $c_i = \pm r c_{\text{max}}$ and $d_i = \pm r' d_{\text{max}}$, where r and r' are random numbers chosen from a uniform distribution on the interval $(0, 1)$, the signs were also chosen randomly, and c_{max} and d_{max} are maximum allowed values ($c_{\text{max}} = 0.03$ a.u. and $d_{\text{max}} = 0.12$ a.u.). A different random number was used when each new coefficient was calculated. The coupling coefficients were altered every $\Delta_r = 20$ time steps (0.48 fs). Figure 9(b) shows the time dependence of the (y_0, y_1) coordinate pair for five trajectories launched from the same initial conditions as those in Fig. 9(a). Compared with the trajectories in Fig. 9(a), these trajectories remain more localized in the region near or before the barrier; excursions into the asymptotic valley are delayed.

C. The $M=15$ direct decay model

Limited computational results will be reported for the $M=15$ direct (barrier-free) dissociative model using the bilinear (nonrandom) coupling Hamiltonian in Eq. (3). In contrast to the potential used for the $M=10$ model, the potential V_2 given in Eq. (5) lacks a barrier along the y_0 coordinate. Parameters used in the Hamiltonian for this model are listed in Table III. The bath mode frequencies ω_i range from 450 to 6000 cm^{-1} and the masses m_i range from 1000 to about 1700 a.u. The CPU time for this model is 76 sec per time step, about 11.5 times larger than the CPU time required for the $M=10$ model. For the 15 bath mode model, $N=201$ trajectories were used to discretize the initial wave packet.

The configuration space-time evolution for two trajectories from the ensemble is shown in Fig. 10(a). Similar to the trajectory plots shown earlier in Figs. 6 and 9, this figure shows the time dependence of the (y_0, y_1) coordinate pair for trajectories 120 and 160. Both of these trajectories move to relatively large values of y_0 by about $t=10$ fs, although trajectory 160 temporarily slows down near $t=6$ fs. Along each trajectory, the total energy (E_{tot}) may be partitioned into

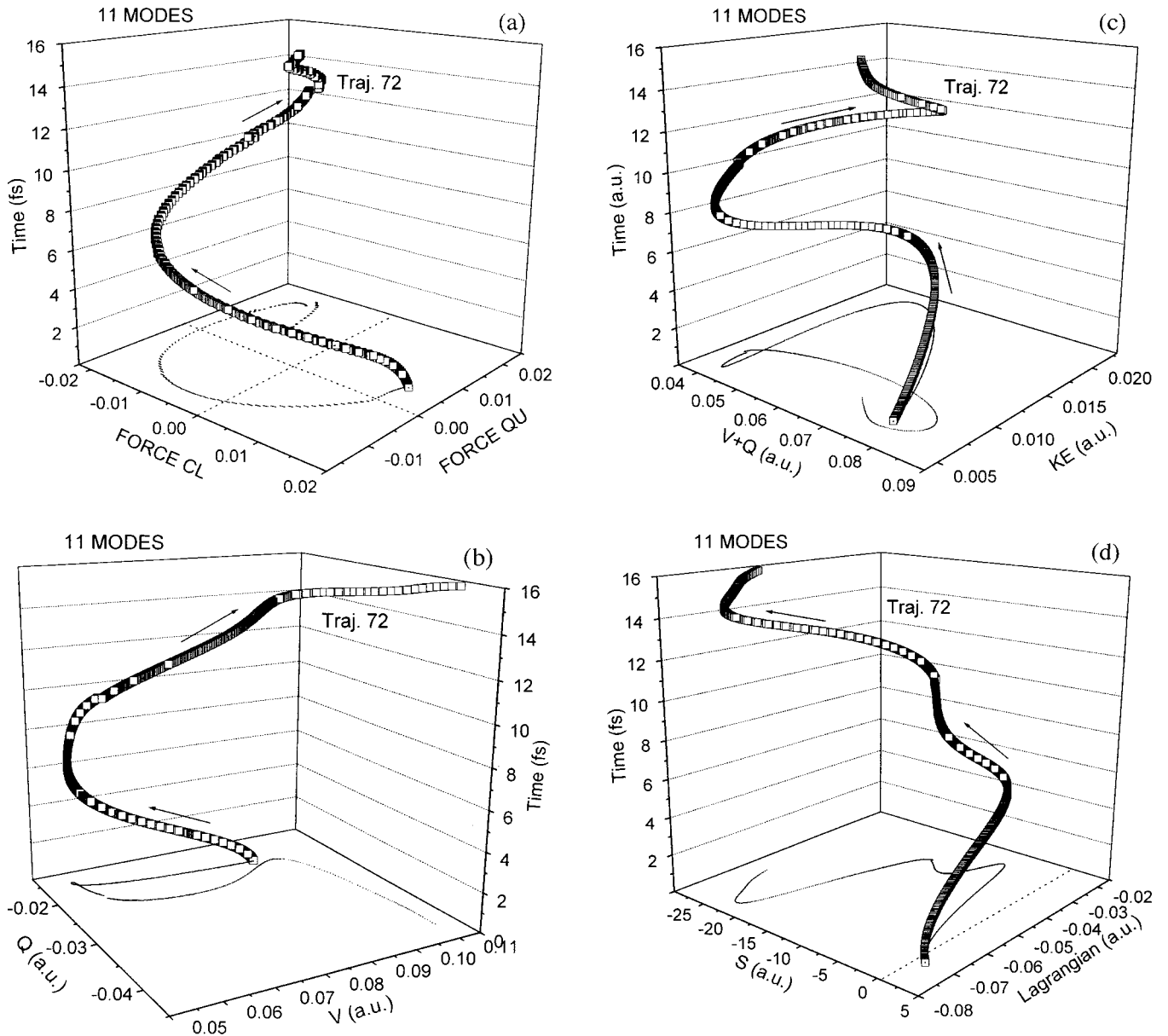


FIG. 8. Dynamical results for trajectory 72: (a) time dependence of the y_0 components of the classical and quantum forces, (b) classical (V) and quantum (Q) potential energies, (c) total potential energy ($V+Q$) and kinetic energy (KE), (d) action function (S) and quantum Lagrangian (L_{quantum}).

subsystem (E_{system}) and bath (E_{bath}) components. (There is some ambiguity about where to put the coupling energy, but for this study, it was included in with the bath energy.) For this trajectory, the fraction of energy in the subsystem is then $f_{\text{system}} = E_{\text{system}}/E_{\text{tot}}$. Figure 10(b) shows the time dependence of the two fractions f_{system} and $f_{\text{bath}} (= 1 - f_{\text{system}})$ for trajectory 72. At early times, the subsystem energy increases slightly, but for later times ($t > 8$ fs) most of the energy has migrated into the 15 bath modes.

V. CONCLUSIONS

The quantum trajectory method had been applied to multidimensional systems consisting of an active mode, the subsystem, interacting with a bath of M uncoupled harmonic oscillators. In this approach, the time-dependent dynamics of

elements of the probability fluid are obtained by integrating the quantum hydrodynamic equations in the Lagrangian picture of fluid mechanics. Along each quantum trajectory, the wave function may be computed, which in addition to the time evolving density, flow velocity, action function, and the classical and quantum forces leads to a detailed, mechanistic, description of the dynamics. As quantum trajectories for these and other related models are computed and analyzed using the quantum hydrodynamic approach, it is likely that new insights will arise and that new approximations will be suggested.

The three systems chosen for analysis in this study have the common feature that wave function nodes do not form during passage of the wave packet from small to large values of the subsystem coordinate. If nodal surfaces were to form, the computational analysis would become more complicated

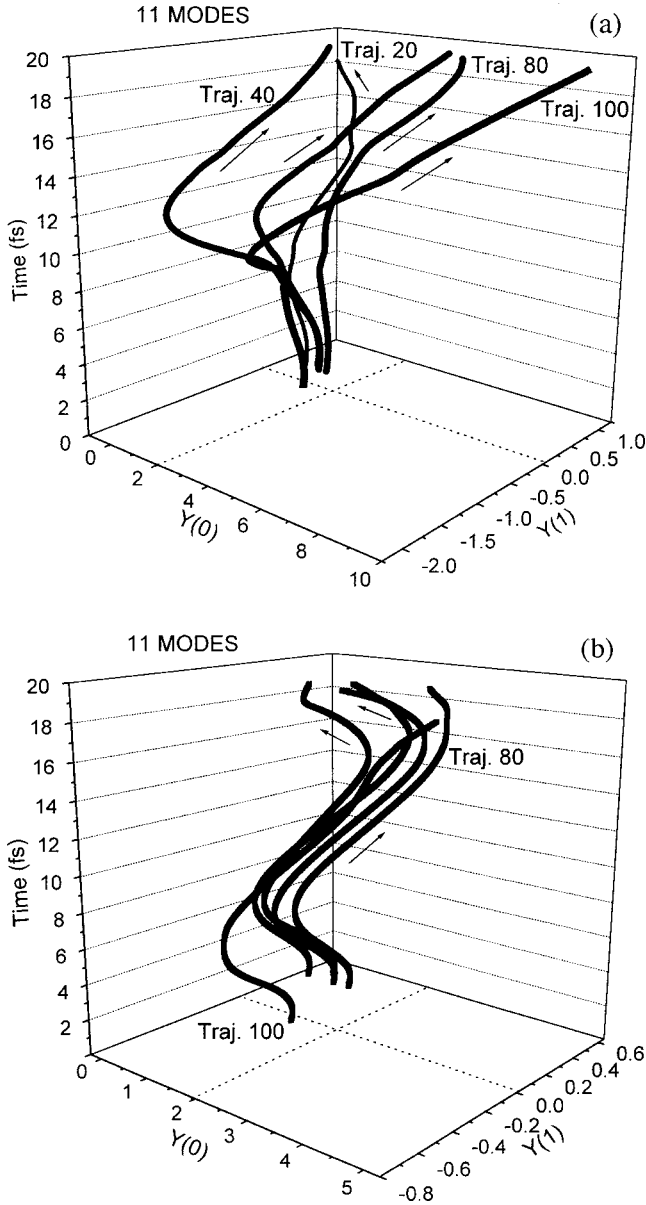


FIG. 9. Time dependence of trajectories 20, 40, 60, 80, and 100 in the (y_0, y_1) plane. Trajectory 100 is associated with a fluid element near the front edge of the wave packet. (a) The subsystem-bath coupling includes (time-independent) bilinear and cubic terms. (b) The bilinear and cubic coupling coefficients are randomized every 0.48 fs.

and some of the techniques (such as adaptive remeshing) discussed recently by Wyatt and Bittner [29] could be used to propagate the fluid elements. In spite of this, there are likely a number of multidimensional systems where node formation is not a dominant feature and for these the quantum hydrodynamic equations presented here will be a viable way to obtain accurate quantum mechanical results without invoking dynamical approximations (such as the quantum subsystem/classical-bath model).

Additional results on subsystem-bath dynamics (influence

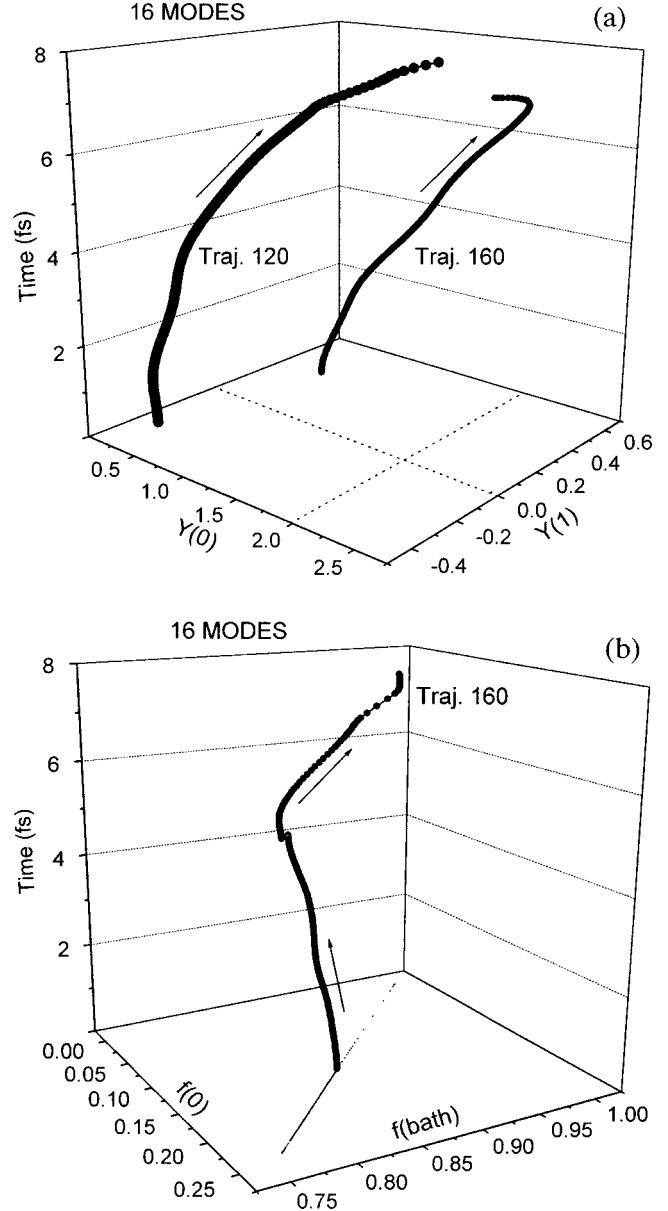


FIG. 10. The $M=15$ bath mode model. (a) Time dependence of trajectories 120 and 160 in the (y_0, y_1) plane. (b) Energy partitioning the time dependence of the fraction of energy in the subsystem and the fraction in the bath are shown for trajectory 160.

of the bath spectral density, dissipation of energy and phase from the subsystem, decoherence, and dynamical averages) will be presented in other parts of this series [63].

ACKNOWLEDGMENTS

This research was supported in part by the Robert Welch Foundation and the National Science Foundation. We appreciate comments from Professor Eric Bittner (University of Houston). We also thank the Texas Advanced Computing Center for providing access to *aurora*, the Cray SV1.

- [1] U. Weiss, *Quantum Dissipative Systems* (World Scientific, Singapore, 1999), pp. 17–20.
- [2] J. Shao and N. Makri, *J. Phys. Chem. A* **103**, 7753 (1999).
- [3] M. Topaler and N. Makri, *J. Chem. Phys.* **101**, 7500 (1994).
- [4] M. Thoss, H. Wang, and W. H. Miller, *J. Chem. Phys.* **114**, 9220 (2001).
- [5] R. Gelabert, X. Gimenez, M. Thoss, H. Wang, and W. H. Miller, *J. Chem. Phys.* **114**, 2572 (2001).
- [6] H. Wang, M. Thoss, and W. H. Miller, *J. Chem. Phys.* **112**, 47 (2000).
- [7] A. O. Caldeira and A. J. Legget, *Physica A* **121**, 587 (1983).
- [8] A. O. Caldeira and A. J. Legget, *Ann. Phys. (N.Y.)* **149**, 374 (1983).
- [9] H. Grabert, P. Schramm, and G. L. Ingold, *Phys. Rep.* **168**, 115 (1988).
- [10] J. Cao, L. W. Ungar, and G. A. Voth, *J. Chem. Phys.* **104**, 4189 (1996).
- [11] D. F. Walls and G. J. Milburn, *Phys. Rev. A* **31**, 2403 (1985).
- [12] C. M. Savage and D. F. Walls, *Phys. Rev. A* **32**, 2316 (1985).
- [13] B. L. Hu, J. P. Paz, and Y. Zhang, *Phys. Rev. D* **45**, 2843 (1992).
- [14] J. P. Paz, S. Habib, and W. H. Zurek, *Phys. Rev. D* **47**, 488 (1993).
- [15] E. G. Petrov, *Phys. Rev. E* **57**, 94 (1998).
- [16] G. Stock, *Phys. Rev. E* **51**, 3038 (1995).
- [17] V. E. Madelung, *Z. Phys.* **40**, 322 (1926).
- [18] L. de Broglie, *An Introduction to the Study of Wave Mechanics* (Dutton, New York, 1930).
- [19] D. Bohm, *Phys. Rev.* **85**, 167 (1952); **85**, 180 (1952).
- [20] D. Bohm and B. J. Hiley, *The Undivided Universe* (Routledge, London, 1993).
- [21] C. Philippidis, C. Dewdney, and B. J. Hiley, *Nuovo Cimento Soc. Ital. Fis., B* **52B**, 15 (1979).
- [22] P. R. Holland, *The Quantum Theory of Motion* (Cambridge University Press, New York, 1993).
- [23] C. L. Lopreore and R. E. Wyatt, *Phys. Rev. Lett.* **82**, 5190 (1999).
- [24] R. E. Wyatt, *Chem. Phys. Lett.* **313**, 189 (1999).
- [25] R. E. Wyatt, *J. Chem. Phys.* **111**, 4406 (1999).
- [26] R. E. Wyatt, D. J. Kouri, and D. K. Hoffman, *J. Chem. Phys.* **112**, 10 730 (2000).
- [27] C. L. Lopreore and R. E. Wyatt, *Chem. Phys. Lett.* **325**, 73 (2000).
- [28] E. R. Bittner and R. E. Wyatt, *J. Chem. Phys.* **113**, 8888 (2000).
- [29] R. E. Wyatt and E. R. Bittner, *J. Chem. Phys.* **113**, 8898 (2000).
- [30] K. Na and R. E. Wyatt, *Int. J. Quantum Chem.* **81**, 206 (2001).
- [31] R. E. Wyatt, C. L. Lopreore, and G. Parlant, *J. Chem. Phys.* **114**, 5113 (2001).
- [32] C. L. Lopreore and R. E. Wyatt (unpublished).
- [33] O. F. de Alcantara Bonfim, J. Florencio, and F. C. Sa Barreto, *Phys. Rev. E* **58**, 6851 (1998).
- [34] S. Sengupta and P. K. Chattaraj, *Phys. Lett. A* **215**, 119 (1996).
- [35] H. Frisk, *Phys. Lett. A* **227**, 139 (1997).
- [36] R. H. Parmenter and R. W. Valentine, *Phys. Lett. A* **201**, 1 (1995).
- [37] Z. S. Wang, G. R. Darling, and S. Holloway (unpublished).
- [38] H. Carlsen, E. Sjoqvist, and O. Goscinski, *Int. J. Quantum Chem.* **75**, 409 (1999).
- [39] H. Carlsen and O. Goscinski, *Phys. Rev. A* **59**, 1063 (1999).
- [40] P. Lancaster and K. Salkauskas, *Curve and Surface Fitting* (Academic, New York, 1986).
- [41] P. Lancaster and K. Salkauskas, *Math. Comput.* **37**, 141 (1981).
- [42] T. Belytschko, Y. Y. Lu, and L. Gu, *Int. J. Numer. Methods Eng.* **37**, 229 (1994).
- [43] B. Nayroles, G. Touzot, and P. Villon, *Computational Mech., Berlin* **10**, 307 (1992).
- [44] D. K. Hoffman, T. L. Marchioro II, M. Arnold, Y. Huang, W. Zhu, and D. J. Kouri, *J. Math. Chem.* **20**, 117 (1996).
- [45] N. Pinto-Neto and E. Sergio Santini, *Phys. Rev. D* **59**, 123517 (1999).
- [46] D. K. Dey, A. Askar, and H. A. Rabitz, *J. Chem. Phys.* **109**, 8770 (1998).
- [47] D. K. Dey, A. Askar, and H. A. Rabitz, *Chem. Phys. Lett.* **297**, 247 (1998).
- [48] F. Sales Mayor, A. Askar, and H. A. Rabitz, *J. Chem. Phys.* **111**, 2423 (1999).
- [49] B. K. Dey, H. A. Rabitz, and A. Askar, *Phys. Rev. A* **61**, 043412 (2000).
- [50] X. G. Hu, T. S. Ho, and H. A. Rabitz, *Phys. Rev. E* **61**, 5967 (2000).
- [51] J. H. Weiner and Y. Partom, *Phys. Rev.* **187**, 1134 (1969).
- [52] J. H. Weiner and Y. Partom, *Phys. Rev. B* **1**, 1533 (1970).
- [53] J. H. Weiner and A. Askar, *J. Chem. Phys.* **54**, 1108 (1971); **54**, 3534 (1971).
- [54] A. Askar and J. H. Weiner, *Am. J. Phys.* **39**, 1230 (1971).
- [55] H. Y. Kim and J. H. Weiner, *Phys. Rev. B* **7**, 1353 (1973).
- [56] J. Maddox and E. R. Bittner, *J. Chem. Phys.* **115**, 6309 (2001).
- [57] E. R. Bittner, *J. Chem. Phys.* **112**, 9703 (2000).
- [58] D. Nerukh and J. H. Frederick, *Chem. Phys. Lett.* **332**, 145 (2000).
- [59] E. Gindensperger, C. Meier, and J. A. Beswick, *J. Chem. Phys.* **113**, 9369 (2000).
- [60] O. V. Prezhdo and C. Brooksby, *Phys. Rev. Lett.* **86**, 3215 (2001).
- [61] J. C. Burant and J. C. Tully, *J. Chem. Phys.* **112**, 6097 (2000).
- [62] G. D. Billing, *J. Chem. Phys.* **114**, 6641 (2001).
- [63] K. Na and R. E. Wyatt (unpublished).